Available online at www.sciencedirect.com

jmr&t Journal of Materials Research and Technology

journal homepage: www.elsevier.com/locate/jmrt

Original Article

Design of tough, ductile direct quenched and partitioned advanced high-strength steel with tailored silicon content

Sumit Ghosh[*], *Pentti Kaikkonen*, *Vahid Javaheri*, *Antti Kaijalainen*, *Ilkka Miettunen*, *Mahesh Somani*, *Jukka Kömi*, *Sakari Pallaspuro*

Materials and Mechanical Engineering, Centre for Advanced Steels Research, University of Oulu, 90014 Oulun Yliopisto, Finland

ARTICLE INFO

Article history:
Received 3 December 2021
Accepted 17 January 2022
Available online 23 January 2022

Keywords:
Direct quenching and partitioning
Dilatometry
Retained austenite
Tempered martensite
Mechanical stability
Toughness

ABSTRACT

The novel processing concept of direct quenching and partitioning (DQ&P) has been explored with a medium-carbon (0.4 wt.% C) steel to evaluate and optimize the processing route for excellent property combinations. New compositional design approach was based on physical simulation studies aiming to understand the influence of varying silicon contents (1.5, 0.75 and 0.25 wt.%) and Q&P processing parameters on microstructural development including carbide formation and retained austenite stabilization. Optimized Q&P parameters were selected to design a DQ&P processing route for laboratory hot-rolling trials based on the analyses of physical simulation data. The overall aim of the study was to produce ultrahigh-strength structural steels with yield strength ≥1100 MPa combined with high uniform and total elongation and impact toughness, achieved through designing a low-temperature quenching and partitioning route with effective carbon partitioning. The DQ&P steels gained an excellent combination of mechanical properties comprising of high yield strength of ~1000–1200 MPa and tensile strength ~2100–2300 MPa, good elongation (~11–13%), and moderate impact toughness transition temperature T_{28J} ~ (−5 to +12 °C). Straining of austenite prior to DQ&P led to an extensive refinement of the final martensitic-austenitic nanostructure. Formation of nanoscale lath-martensite and fine film-like retained austenite structures enabled the observed improvement of mechanical properties. Besides the formation of nano-twinned martensite, inter-lath austenite and transitional carbides were comprehensively characterized. No adverse effect of prolonged partitioning during slow cooling, simulating coiling in actual industrial practice, has been noticed suggesting new possibilities for developing tough, ductile structural steels both for strip/plate products.

* Corresponding author.
E-mail address: sumit.ghosh@oulu.fi (S. Ghosh).

https://doi.org/10.1016/j.jmrt.2022.01.073

1. Introduction

There has been an ever-increasing demand for developing ultrahigh strength steels with excellent combinations of mechanical and usability properties, such as high strength, good ductility, adequate low-temperature toughness and reasonable formability. However, this requires an optimal design of both lean, inexpensive compositions as well as thermomechanical processing (TMP) routes in order to meet the demanding challenges. In this context, quenching and tempering (Q&T) treatment has been known to impart reasonable toughness besides acceptable ductility in high-strength structural steels. All the same, their uniform elongation, i.e., the strain hardening capacity prior to the onset of necking is relatively low. This inadequacy is an important criterion limiting the broader application of quenched and tempered steels, because strain localization during fabrication of components or as a result of overloading in service can be detrimental to the integrity of the structure. In recent years, the concept of quenching and partitioning (Q&P) has been widely accepted as a potential processing route in improving the balance of elongation to fracture and tensile strength of advanced high-strength steels [1–4].

The Q&P process has been originally proposed by Speer et al. [1] in 2003, whereby the steel is austenitized, quenched to a temperature (denoted as T_Q) between the martensite start (M_s) and finish (M_f) temperatures and then immediately held at a desired partitioning temperature (denoted as T_P; often $\geq T_Q$) for a suitable time (P_t) to allow the partitioning of carbon from supersaturated martensite to austenite, which can thereby be partly or fully stabilized down to room temperature [2–6]. Unlike in the case of tempering, the formation of iron carbides and/or decomposition of austenite are purposefully suppressed by the use of Si or Al alloying, similarly as in the case of transformation-induced plasticity (TRIP) steels [2–6]. Austenite stabilized down to room temperature (RT) is often finely divided as thin interlath films or as smalls pools between the martensite blocks. Whilst the martensitic matrix has the potential to provide the required high strength, a small fraction of finely divided austenite stabilized between the martensitic laths is expected to provide the desired uniform elongation and work hardening characteristics via the TRIP effect [7–10].

Austenite retained after the final cooling to room temperature depends not only on the T_Q i.e., the amount of primary martensite but also on the T_P and P_t. Some austenite may transform to fresh martensite during final cooling depending on its carbon enrichment, which can expectedly vary from one location to another, often with concentration gradients in the pools or interlath films [11]. This type of untempered, high carbon martensite is often referred to as the secondary martensite (SM). This brittle untempered martensite possesses potentially high hardness and may often have different deformation behaviour owing to its high carbon content compared to the prior athermal martensite [12]. Besides partitioning, there are a host of other microstructural mechanisms that take place during Q&P processing, such as precipitation of carbides, tempering of martensite, as well as phase transformation to bainite [13,14]. Few studies have even suggested the formation of isothermal martensite in Q&P steels [15–17]. Kim et al. [17] contributed extensively to the understanding of isothermal martensite transformation of a CMnSi steel below the M_s temperature, illustrating its main differences from conventional athermal martensite using electron microscopy and internal friction measurements. The occurrence of potentially different microstructural processes either in parallel or in succession during Q&P processing render the evolved microstructure very complex.

Using a thermomechanical simulator (such as the Gleeble), which is equipped with a dilatometer it is possible to record the dimensional changes (representative of volumetric changes) in steel samples during the Q&P process. In principle, a careful analysis of the dilatometric data may enable *in situ* correlation with the operating microstructural mechanisms [18–20]. For instance, carbon partitioning leads to a very small volume expansion [20–24]. Potential isothermal phase transformation of austenite to bainite (or martensite) leads to an appreciable volume expansion that can be recorded by linear dimensional changes. On the other hand, tempering of martensite leads to gradual contraction [20–24]. Kim et al. [25] have studied the role of silicon using 1% C experimental steels without or with 2% Si. According to their research, carbide precipitation takes place regardless of the silicon content, but the addition of silicon does stabilize the austenite and retard the decomposition process. Ni is generally added to the steels to help in stabilizing austenite and for its positive influence on elongation and toughness [26].

Based on the physical and laboratory rolling simulations of Q&P processing, a novel direct quenching and partitioning (DQ&P) process has recently been proposed by Somani et al. [2,9]. The specific aim of this study was to develop a steel with yield strength of the order of ~1100 MPa combined with good ductility and impact toughness. DQ&P consists of thermomechanical rolling in two stages. In the first stage, recrystallization controlled rolling was carried out in the hot rolling regime in a number of passes. The second stage comprised was rolling in no-recrystallization (T_{nr}) regime to produce adequate straining in austenite before direct-quenching to a desired T_Q in the M_s-M_f range, followed by partitioning for a given duration at the same temperature as T_Q (= T_P) or by very slow cooling in a furnace over 29–30 h. It has been demonstrated that for suitably designed 0.2 wt.% C steels, DQ&P processing could impart high mechanical properties with ~1100 MPa yield strength with good low temperature toughness and reasonable uniform and total elongations [2,9]. Similarly, Kantanen et al. [10] have reported very promising results in DQ&P processing of 0.3% C steels with excellent mechanical properties. High yield strength is attributed to the extensive refinement and high dislocation density of the martensite. In addition, on tempering, precipitation of very fine carbides in heavily dislocated laths additionally enhances the strength. On the other hand, improved toughness is associated with the shortening and randomization of the martensitic laths achieved via ausforming in the T_{nr} regime leading to extensive pancaking of the austenite grains prior to DQ&P processing. Overall, DQ&P could offer a wider range of possibilities for achieving a good combinations of mechanical properties via appropriate thermomechanical controlled rolling including adequate ausforming in the T_{nr} regime prior to quenching and partitioning.

Although, the structural mechanisms operating during the Q&P process as a function of processing variables have been broadly discerned through dilatometry measurements and reported in the literature [20], a systematic investigation of the effect of straining in austenite within the T_{nr} regime on the subsequent Q&P behaviour and possible decomposition of austenite into isothermal martensite and/or bainite and carbide formation, if any, have not been systematically illustrated, particularly with respect to medium carbon steels. Moreover, the effect of Si on austenite decomposition after straining and other mechanisms operating during carbon partitioning have not been investigated in detail. To clarify some of these issues, this study was aimed at investigating the associated microstructural mechanisms during DQ&P processing of 0.4 wt.% C steels with varying Si levels using dilatometric analysis with the aid of physical simulation on a Gleeble simulator. The objectives of the investigation were to unravel the influence of composition design and processing parameters on subsequent dilatation behaviour, microstructural evolution, nature and type of carbide formation, RA stabilization and concerned morphology as well as carbon content aspects. The nature of the dilatometric curves was comprehended carefully and illustrated together with microstructural features to discern the operating microstructural mechanisms. Based on the Gleeble simulated results, suitable thermo-mechanical rolling processes were designed for laboratory rolling simulations, followed by DQ&P processing. The DQ&P samples were characterized and evaluated in respect of microstructures and mechanical properties. Additionally, the mechanical stability of the retained austenite was characterized by performing interrupted tensile tests at different levels of strain and determining the corresponding retained austenite fractions through XRD analysis. This paper presents a first detailed account of the salient results encompassing the dilatation behavior, hot rolling aspects, various microstructural mechanisms including carbide formation and related mechanical properties obtained on 0.4 wt.% C DQ&P processed steels with varied Si contents.

2. Materials and methods

2.1. Test materials and Q&P simulations

Three medium carbon (0.4 wt.% C) steels containing fixed contents of 2 wt.% Mn, 1.0 wt.% Cr and 0.5 wt.% Ni, and a varied level of Si (i.e., 1.5, 0.75 and 0.25 wt.%) were designed for this study. The steel castings were procured from OCAS NV, Zelzate, Belgium as 70 kg vacuum-cast ingots. The final compositions of the experimental steels determined using the spark-optical emission spectroscopy (SOES) and combustion analysis for carbon are presented in Table 1. All percentages mentioned here onwards depict wt.%, unless specified.

Blocks of dimensions 120 × 80 × 60 mm cut from these experimental castings were soaked at 1200 °C for 2 h and hot rolled to 12 mm thick plates using a laboratory rolling mill. Cylindrical specimens of dimensions φ 6 × 9 mm were machined with the axis of the cylinders transverse to the rolling direction in the rolling plane for conducting Q&P experiments on prior strained specimens in a Gleeble 3800 thermomechanical simulator. Prior to Q&P simulations, one specimen from each steel was reheated at 20 °C/s to 1150 °C, held for 2 min and then cooled at 5 °C/s to 850 °C prior to straining. The samples were held at 850 °C for 10 s and then compressed with three hits each having a strain of ~0.2 at a strain rate of 1 s^{-1} (3 × 0.2 strain) prior to cooling to room temperature (RT) at 30 °C/s. Dilatation measurements were made throughout the cooling right from the austenitizing temperature followed by subsequent Q&P treatments, as described below. The accuracy of the dilatometer in Gleeble is stated to be ±0.25% on the full scale according to the manufacturer and the corresponding resolution is 0.4 μm. The accuracy of the temperature measurement is at least ±1% and the resolution is 1 °C. A linear cooling rate of 30 °C/s was selected based on the predictions of the CCT diagrams plotted using the commercial JMatPro 8.0® software in order to avoid phase transformation prior to reaching the M_s temperature. The results estimated ~99% martensitic microstructure with ~1% retained austenite at a cooling rate of 30 °C/s for all steels.

Table 1 – Chemical compositions and M_s temperatures of the test materials.

Steel code	C [%]	Si [%]	Mn [%]	Al [%]	Cr [%]	Ni [%]	M_s [°C]
High-Si	0.40	1.51	2.05	0.02	1.00	0.49	260
Med-Si	0.40	0.68	2.04	0.02	1.00	0.49	275
Low-Si	0.40	0.25	2.02	0.02	1.00	0.49	280

Regardless of the steel composition, Q&P simulations were designed with the quench stop or quenching temperature $T_Q = 150$ °C selected based on the linear analysis of the dilatation curves to obtain ~80% of primary martensite prior to partitioning. A partitioning temperature (T_P) of ~200 °C was selected with an optimal partitioning time (P_t) of ~1000 s based on our previous study [20]. In order to study the influence of Si content on the occurrence of microstructural mechanisms, one particular partitioning time ($P_t = 1000$s) was selected in the present study, both for High-, Med- and Low-Si steels. The main reason behind the selection of a relatively low partitioning temperature was to avoid excessive austenite decomposition (bainitic transformation) and/or carbide formation/growth during isothermal holding at 200 °C. Prior to quenching from the austenitization temperature, the specimens were subjected to 3 × 0.2 prior straining at ~850 °C, as described above. Subsequently, the change in specimen diameter during cooling was recorded with a dilatometer. A schematic diagram of the Q&P simulation plan is presented in Fig. 1, showing the reheating, prior 3 × 0.2 straining, cooling and partitioning steps, including various heating and cooling rates. A detailed analysis of the dilatation measurements made on Gleeble simulated Q&P samples enabled selection of appropriate Q&P schedules for subsequent design of DQ&P process using the laboratory rolling mill.

Based on the results of the Q&P simulations in the Gleeble, direct quenching and partitioning (DQ&P) schedules were designed, as displayed schematically in Fig. 2. Rolling trials were performed in a two-high, reversing laboratory rolling mill with blocks of 120 × 80 × 60 mm cut from cast ingots. The temperature of the samples during rolling and quenching was monitored by thermocouples placed in holes drilled in the

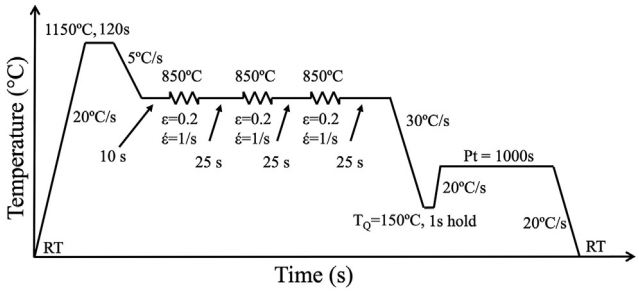

Fig. 1 – Schematic schedule of the Gleeble Q&P simulations.

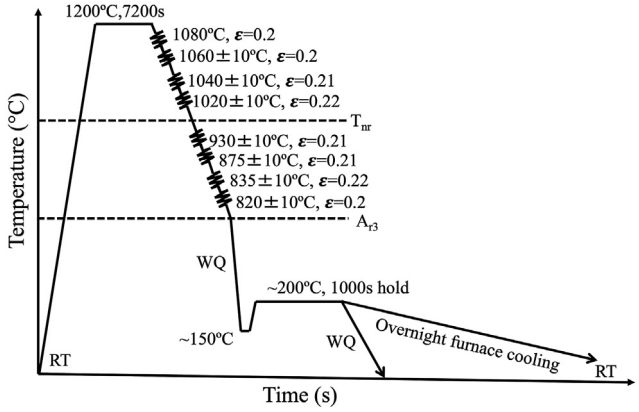

Fig. 2 – Laboratory rolling process followed by DQ&P treatment.

edges of the samples to the mid-width at mid-length. Referring to Fig. 2, the samples were soaked at 1200 °C for 2 h in a furnace prior to two-stage rolling. In the first stage, hot rolling was carried out in the recrystallization regime in 4 passes to a thickness of 26 mm with about 0.2 strain/pass with the temperature of the fourth pass at about 1020 ± 10 °C. The second stage comprised waiting for the temperature to drop to ≈930 ± 10 °C and then rolling in no-recrystallization regime to a thickness of ~11 mm with 4 passes of ~0.2 strain/pass and a finish rolling temperature (FRT) at about ≈820 ± 10 °C. Following thermomechanically controlled rolling to 11 mm thick plates, the samples were immediately quenched in a tank of water close to the desired T_Q of 150 °C and then subjected to partitioning treatment in a furnace maintained at T_P of 200 °C. While one plate of each steel was held at T_P for the partitioning time (P_t) of 1000 s, the other plates, processed under similar conditions, were cooled very slowly over ~24 h by switching off the furnace in order to simulate the cooling of the coiled strips in actual industrial practice. The furnace temperature dropped to ~80 °C within the 24 h period.

2.2. *Characterization*

All the Gleeble specimens were sectioned in the middle along the length of the samples (i.e., parallel to the compression axis) close to the thermocouple location, for microstructural characterization. In case of DQ&P plates, the specimens were extracted in the plane of the RD-ND (rolling direction – normal direction) cross-section. All the samples were polished in accord with ASTM E3-11 standard metallographic procedure, followed by etching using 2% Nital reagent, and the microstructural examination was conducted in a Zeiss Sigma field-emission scanning electron microscope (FE-SEM). Select specimens were investigated in depth using an electron back scattered diffraction (EBSD) facility equipped with the FE-SEM to reveal the phase distribution including RA, though limited by the resolution of the technique (about 0.08 μm). The specimens for EBSD measurements were prepared involving an additional polishing step using colloidal silica (0.004 mm) suspension, following the standard metallographic polishing. The EBSD analysis was performed with the help of a HKL channel-5 system software. The EBSD data measured on laboratory rolled specimens were further processed to reconstruct the prior austenite grains in order to measure the prior austenite grain size (PAGS) using MTEX toolbox in MATLAB™ software [27,28]. A detailed description of the analytical method and its reliability are presented elsewhere by Nyyssönen et al. [27].

Transmission electron microscopy (TEM) study was conducted using a JEOL 2200FS EFTEM/STEM operated at 200 kV enabling high magnification resolution to illustrate in-depth structural phenomena that might be occurring during DQ&P processing. For TEM analyses, thin lamellas were sectioned from the specimens using focused ion beam (FIB) technique. The volume fraction of retained austenite was determined using a Rigaku Smart Lab 9 kW XRD unit (40 kV; 135 mA). The measurements were performed using CoK_a X-rays with 2θ ranging between 45° and 130° and the rotation performed at 7.2°/min. The obtained diffractograms were analysed by Rietveld refinement using a PDXL2 software. The carbon content of the retained austenite (C_γ) was also estimated based on the lattice parameter of austenite (a_γ) derived from XRD results using the method and equation (Eq. 1) established by Dyson and Holmes [29], where a_γ is the austenite lattice parameter (Å) and x_n are the concentrations (in wt.%) of the respective alloying elements.

$$a_\gamma = 3.556 + 0.0453x_C + 0.00095x_{Mn} + 0.0056x_{Al} + 0.0006x_{Cr} \quad (1)$$

The average HV5 hardness values of the Gleeble specimens were measured using a Duramin A-300 automatic hardness tester (at least 5 indentations per specimen). Tensile tests were performed at the ambient temperature according to ASTM E8M standard on specimens machined in the transverse direction (3 tests per material). A constant true strain rate of 0.008 s^{-1} was employed. Also, interrupted tensile tests were performed for select steel samples (DQ&P furnace cooled High-, Med- and Low-Si steels) at the same strain rate (0.008 s^{-1}) with tests interrupted at engineering strains of 2%, 6% and 10% in order to understand the stability of RA, particularly the mechanical stability. Charpy V impact toughness tests were conducted on standard specimens (size: 10 × 10 × 55 mm^3) machined according to ASTM E23 standard along the longitudinal direction, such that the direction of impacting is transverse to the rolling direction. Charpy V tests were performed in a broad temperature range from −80 °C to +100 °C (2–3 specimens per temperature).

3. Results and discussion

3.1. Dilatometry

Figure 3a presents the dilatation curves depicting percent change in diameter vs. temperature of steel specimens continuously cooled to RT at a linear rate of 30 °C/s following reheating at 1150 °C for 2 min and prior 3 × 0.2 straining at 850 °C, thus simulating direct quenching (Fig. 1). Austenite decomposition into martensite can be ascertained by the inflexions in the curves. The dilatation curves of the Gleeble simulated Q&P specimens for the High-, Med- and Low-Si steels processed according to the test plan given in Fig. 2 are presented in Fig. 3b, showing percent change in diameter following quenching at 150 °C and subsequent reheating and partitioning at 200 °C for 1000 s. After 1 s hold at T_Q, heating to T_P occurs at 20 °C/s, which explains most of the rapid expansion immediately after 1 s. During the heating and at the beginning of the partitioning treatment, there are some electronic control-related oscillations in the dilatometric measurements, which explain the peaks and vibrations seen in the diametric changes [20].

Referring to Fig. 3b, after T_P (=200 °C) is reached, initially a slow gradual increase in diameter is clearly evident on the logarithmic scale (region I) and then a more rapid increase (region II) in all three steels. Unlike High-Si steel, the rapid increase in diameter corresponding to region II is quite prominent in Med- and Low-Si steels. The region I type increase in the diameter is mainly due to carbon partitioning. The scale of increase correlates well with the reported volume expansion due to carbon partitioning alone [19], though formation and migration of ledges that allow the martensite laths to grow into the austenite isothermally is a distinct possibility too [16], though could not be detected in the microstructure. The more significant, however, is the rapid expansion seen in region II type, which has been ascribed to the decomposition of austenite into bainite [18]. In the literature, a third region (region III) has also been reported, in which the steel contracts due to extensive tempering of martensite, as also seen in the case of Low-Si steel, Fig. 3b [16,20].

High-Si steel has a relatively small net increment in diameter as compared to steels B and C, though some fluctuations have been seen between 70-300 s in the dilatation curves essentially due to data acquisition issues. The results in all imply that an addition of 1.5 wt. % silicon in the steel is quite effective in retarding the decomposition of austenite under the given experimental conditions. In Med- and Low-Si steels, a greater change in diameter was recorded during the later stages of partitioning, particularly in the case of Low-Si steel. A small contraction was noticed after 600–700 s of partitioning in the case of Low-Si steel, presumably due to the onset of carbide precipitation accompanying the tempering of

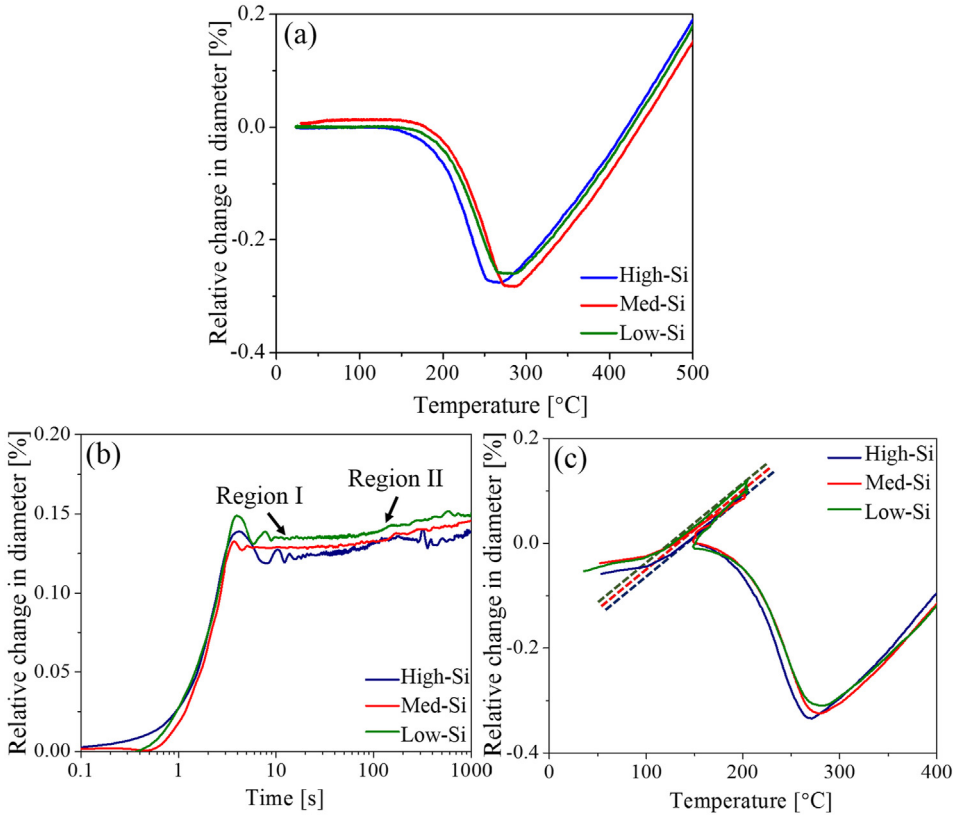

Fig. 3 – a) Dilatation curves of the steel specimens continuously cooled at 30 °C/s to RT following reheating at 1150 °C and 3 × 0.2 straining at 850 °C (b) relative change in diameter vs. time curves plotted for Gleeble-simulated Q&P specimens quenched at 150 °C, followed by partitioning at 200 °C, and c) corresponding dilatation curves depicting percent change in diameter as a function of temperature during continuous cooling and subsequent Q&P treatment (Fig. 1).

martensite despite a relatively low partitioning temperature (200 °C). These findings correlate well with the decomposition behaviour of Q&P steels without or with (2%) silicon, as reported by Kim et al. [25].

Further, the dilatation curves showing percent change in diameter as a function of temperature during cooling and subsequent Q&P processing of the investigated steels are presented in Fig. 3c. These plots reveal not only appreciable change in diameter for Steels B and C in comparison to High-Si steel due to partitioning at 200 °C, but also clearly display formation of untempered, high carbon martensite, also termed as secondary martensite (SM) during final cooling marked by significant inflexions in the curves in a close range of 110–120 °C with appreciable changes in the slopes of the cooling curves. There is a clear evidence of SM formation following partitioning at 200 °C in each of the experimental steels regardless of Si content, suggesting incomplete carbon partitioning at 200 °C despite isothermal holding for 1000 s.

3.2. *XRD and hardness*

Table 2 presents a summary of the RA contents, austenite lattice parameters (a_γ) and carbon content of RA (C_γ) derived from XRD data, for the Q&P/DQ&P simulated Gleeble specimens. Average hardness data (HV5) measured on the samples are also included in the table for the ease of comparison and analysis. It is clearly evident that with a higher Si content, more austenite can be retained in Gleeble simulated Q&P specimens. The highest amount of austenite is retained in High-Si steel (10%) as compared to Med-Si steel (~9%) and Low-Si steel (~5%), though the probability of carbide formation during partitioning at 200 °C is somewhat low. In the case of laboratory rolled DQ&P samples, the difference in RA contents of the three steels was smaller, though the trend was very similar. Based on the dilatometric results of Gleeble simulated Q&P samples, a decisive conclusion of this study is that the isothermal holding of mere 1000 s at the partitioning temperature of 200 °C is perhaps not enough to equilibrate carbon partitioning in austenite and stabilize it, even in the case of High-Si steel with 1.5 wt.% Si, and hence, a fraction of the carbon-enriched austenite would transform to SM during final cooling, as illustrated in Fig. 3c.

The RA contents (measured from the centerline) of the laboratory rolled DQ&P plates with $P_t = 1000$ s were very close to those of Gleeble simulated Q&P specimens processed under similar conditions, including prior 3 × 0.2 straining and Q&P processing (Table 2), indicating that physical simulation has been largely successful in revealing the accompanying mechanisms. On the other hand, the furnace cooled (FC) DQ&P plates have displayed higher fractions of austenite contents compared to those of DQ&P plates controlled partitioning of $P_t = 1000$ s. Again, a high level of Si resulted in stabilizing a high austenite fraction, but only marginally. Even in Low-Si steel with a nominal Si content of mere 0.25% that is normally present in ordinary steels, an appreciable fraction of 11% austenite was retained at RT following the coiling simulation, suggesting that the role of Si in delaying or preventing carbide formation, if any, is probably limited, as the propensity to form carbides at such low partitioning temperatures is limited, too. In comparison, a marginally higher fraction of 15% RA was realized in High-Si steel via furnace cooling. C_γ contents are at a similar level regardless of the steel type, being ~10% higher in the coiled strips (0.59–0.63 wt.% C) compared to 1000 s plates (0.51–0.54 wt.%) suggesting somewhat better stability. Similarly, Gleeble-simulated Q&P specimens showed ~10–20% higher C_γ content in RA compared to those of DQ&P plates, despite limited partitioning time of $P_t = 1000$ s. This is explained by the different stress-state produced by the processing routes [10,30].

In all, a long P_t involving slow furnace cooling has presumably led to adequate partitioning and possible equilibration of carbon in untransformed austenite at 200 °C to prevent further decomposition of carbon-enriched austenite during final cooling. The differences in the RA contents were ~5–6% between the furnace-cooled and 1000 s held plates in all the three steels, regardless of silicon content, suggesting the efficacy of longer holding in stabilizing the carbon-entiched austenite nearly completely. Overall, Si has been effective in promoting carbon partitioning and equilibration, though the effect has been less pronounced compared to what is normally seen at slightly higher Q&P temperatures, whence carbide precipitation/growth and austenite decomposition may compete with the partitioning process.

Table 2 – RA contents (γ), austenite lattice parameters (a_γ) and derived carbon contents of RA (C_γ) measured on Gleeble simulated Q&P and lab rolled DQ&P samples. Hardness data measured on the samples are also included.

Steel code	Processing	γ [%]	a_γ [Å]	C_γ [%]	HV 5
High-Si	Cooled 30 °C/s	8 ± 1	3.580 ± 0.002	0.46 ± 0.03	639 ± 3
	Gleeble Q&P	10 ± 1	3.585 ± 0.002	0.59 ± 0.02	653 ± 5
	DQ&P-1000s	9 ± 1	3.582 ± 0.004	0.51 ± 0.02	662 ± 3
	DQ&P-FC	15 ± 1	3.587 ± 0.003	0.63 ± 0.03	603 ± 4
Med-Si	Cooled 30 °C/s	5 ± 1	3.584 ± 0.004	0.56 ± 0.03	632 ± 3
	Gleeble Q&P	9 ± 1	3.587 ± 0.002	0.62 ± 0.02	634 ± 5
	DQ&P-1000s	8 ± 1	3.583 ± 0.002	0.53 ± 0.02	664 ± 4
	DQ&P-FC	13 ± 1	3.586 ± 0.004	0.59 ± 0.03	598 ± 4
Low-Si	Cooled 30 °C/s	6 ± 1	3.583 ± 0.003	0.54 ± 0.03	635 ± 2
	Gleeble Q&P	5 ± 1	3.590 ± 0.003	0.69 ± 0.03	632 ± 3
	DQ&P-1000s	6 ± 1	3.583 ± 0.002	0.54 ± 0.02	653 ± 3
	DQ&P-FC	11 ± 1	3.586 ± 0.004	0.61 ± 0.03	586 ± 4

The hardness of the Gleeble simulated Q&P/DQ&P steels with P_t = 1000 s (653–664 HV5) expectedly decreased with increasing P_t (586–603 HV5). The hardness also decreased marginally with decreasing Si content despite the fact that the RA contents would also decrease with a concomitant increase in martensite. This is a clear indication of austenite transforming into somewhat softer bainite during partitioning, rather than 'hard' secondary martensite during final cooling, though the data are limited and possibly scattered, too. Also, it is noteworthy that the carbon content of the austenite plays a notable role in its hardness following transformation, whereby a high carbon content translates to relatively high hardness, which explains the fact that the DQ&P-1000s plates partitioned at 200 °C and held for 1000 s have had similar or even higher hardness values (653–664 HV5) than those of the Gleeble Q&P samples and/DQ&P-furnace cooled steels (Q&P: 632–653 HV5; DQ&P-furnace cooled: 586–603 HV5), even though a slight tempering effect is expected to marginally soften the steels. Furthermore, the extent of transition carbide precipitation during low temperature partitioning (at 200 °C) in the case of both Q&P/DQ&P treatments has been found to surge with decreasing Si content (discussed later in Section 3.3.3). The hardness values of the samples that experienced formation of η-carbides were relatively lower, as a result of decrease in carbon content of the martensite and reduced carbon partitioning effect.

3.3. Microstructures

3.3.1. Scanning electron micrography

Secondary electron micrographs of select Gleeble-simulated Q&P specimens are presented in Fig. 4(a-f). Microstructures of all the specimens consisted mainly of fine packets and blocks of martensite and small fractions of fresh martensite/retained austenite islands (M/A) distributed randomly throughout the microstructure. The M/A islands seen in the structures are the former pools of austenite that are only partly transformed to martensite during final cooling. The presence of needle-like transition carbides parallel to specific habit planes within martensite blocks is visible in all steels (Fig. 4b, d and f). The fraction of carbides seen in Low-Si steel is relatively higher compared to the other two steels. Clear traces of bainitic packets are evident in all steel specimens (Fig. 4b, d and f). This observation suggests that even at 200 °C, martensite tempering competes with carbon partitioning and bainite transformation. As also discerned from dilatometry and XRD results, a holding time of P_t = 1000 s at 200 °C was just

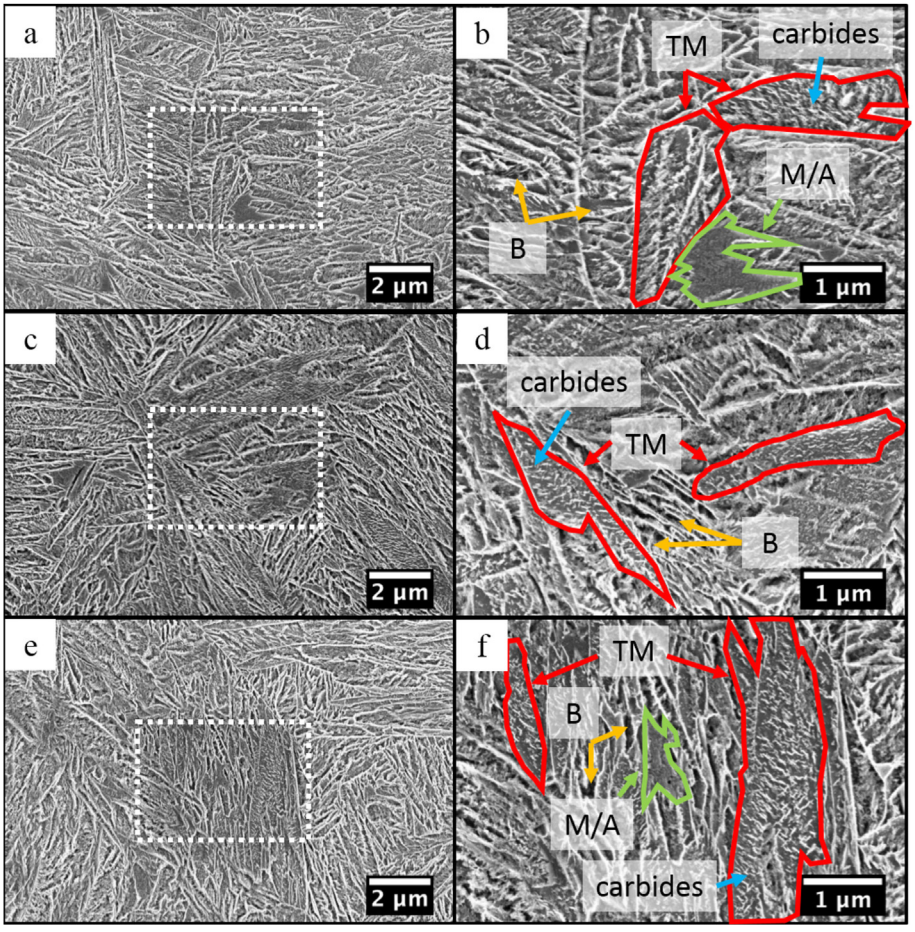

Fig. 4 – SEM micrographs (in-lens) of Gleeble simulated Q&P (T_p = 200 °C) specimens with P_t = 1000 s: High-Si a)-b), Med-Si c)-d), and Low-Si steels e)-f). Magnified view of dashed rectangles in a), c), and e) are shown in b), d), and f), respectively.

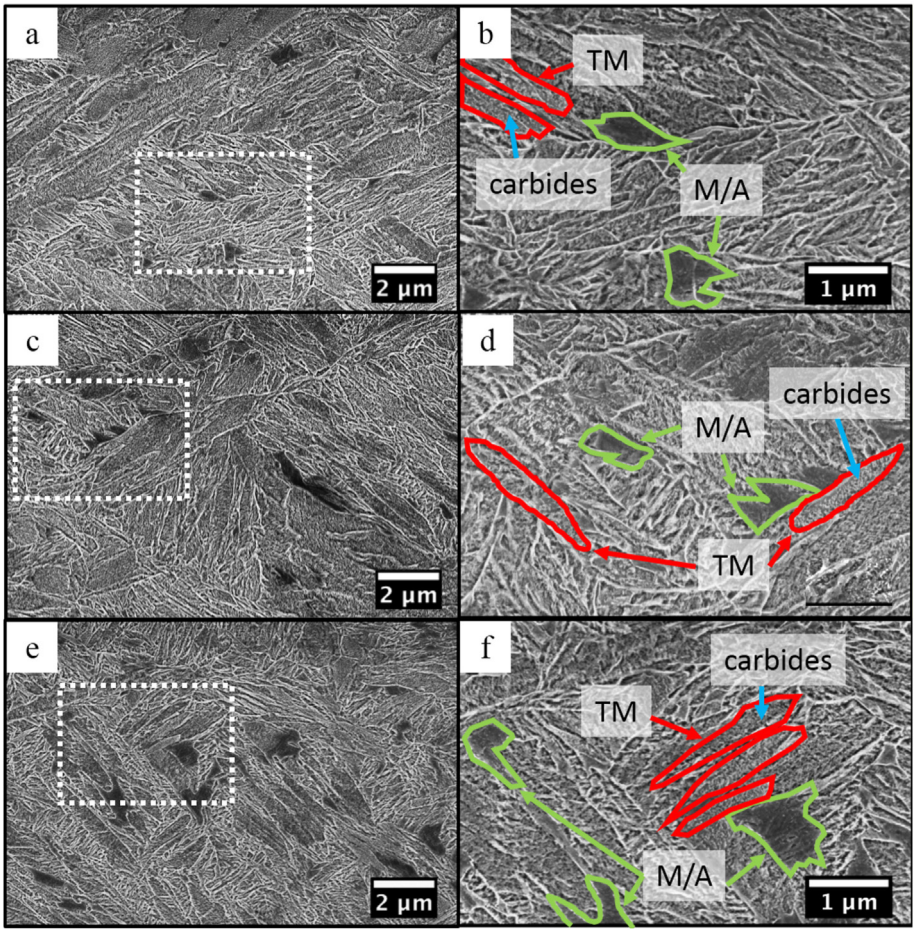

Fig. 5 – SEM micrographs (in-lens) of laboratory rolled DQ&P steels with $P_t = 1000$: High-Si a)-b), Med-Si c)-d), and Low-Si steels e)-f). Magnified view of dashed rectangles in a),c), and e) are shown in b), d), and f), respectively.

not enough to stabilize the RA fully at room temperature regardless of the Si content in the steel.

Secondary electron images of the laboratory rolled DQ&P steel specimens with $P_t = 1000$ s at 200 °C for High-, Med- and Low-Si steels are presented in Fig. 5a, c and d, respectively. So far as microstructures are concerned, there are no appreciable differences between the laboratory rolled DQ&P ($P_t = 1000$ s) and Gleeble simulated Q&P samples (High-, Med- and Low-Si steels).

Secondary electron images of the laboratory rolled DQ&P samples cooled slowly in furnace, simulating industrial coiling practice, are presented in Fig. 6a, c and e for High-, Med- and Low-Si steels, respectively. The furnace-cooled "coiled" variants clearly exhibit regions of tempered martensite (TM) (Fig. 6b, d and f). The microstructures also comprise of significant fractions of M/A constituents, both square-like and elongated, which are in accord with the presence of a high fraction of austenite contents in the furnace-cooled DQ&P samples.

3.3.2. *EBSD analysis*

Fig. 7a, d and g present the reconstructed prior austenite grain structures (PAGs) of the DQ&P-furnace cooled High-, Med- and Low-Si steels, respectively. Fig. 7b, e and h show higher magnification micrographs of the selected regions in Fig. 7a, d and g, respectively. In all cases the reconstructed PAGs showed partially recrystallized grains together with "pancaked" grain structures, presumably as a consequence of deformation in the T_{nr} regimes. The reconstructed PAGs of DQ&P-furnace cooled plates revealed partially recrystallized structures comprising both fine as well as coarse, randomly oriented grains, besides wide grain size distributions ranging from 5 μm to 50 μm, as depicted in Fig. 7c, f and i. The grain size has been estimated based on the equivalent circle diameters (ECD) of the grains and corresponding histograms of the relative fractions are shown as bar charts in Fig. 7c, f and i. The average PAGs sizes varied in a narrow range and were estimated to be ~18–20 μm.

To investigate further about the orientation relationship and to differentiate martensite from austenite, a high resolution EBSD analysis was conducted. It is well known that the martensite formed from austenite following water quenching is accompanied by lattice distortion and thereby accommodates high density of dislocations. Although, recovery of dislocations via movement and annihilation (tempering) does occur alongside partitioning, still a high density of dislocations

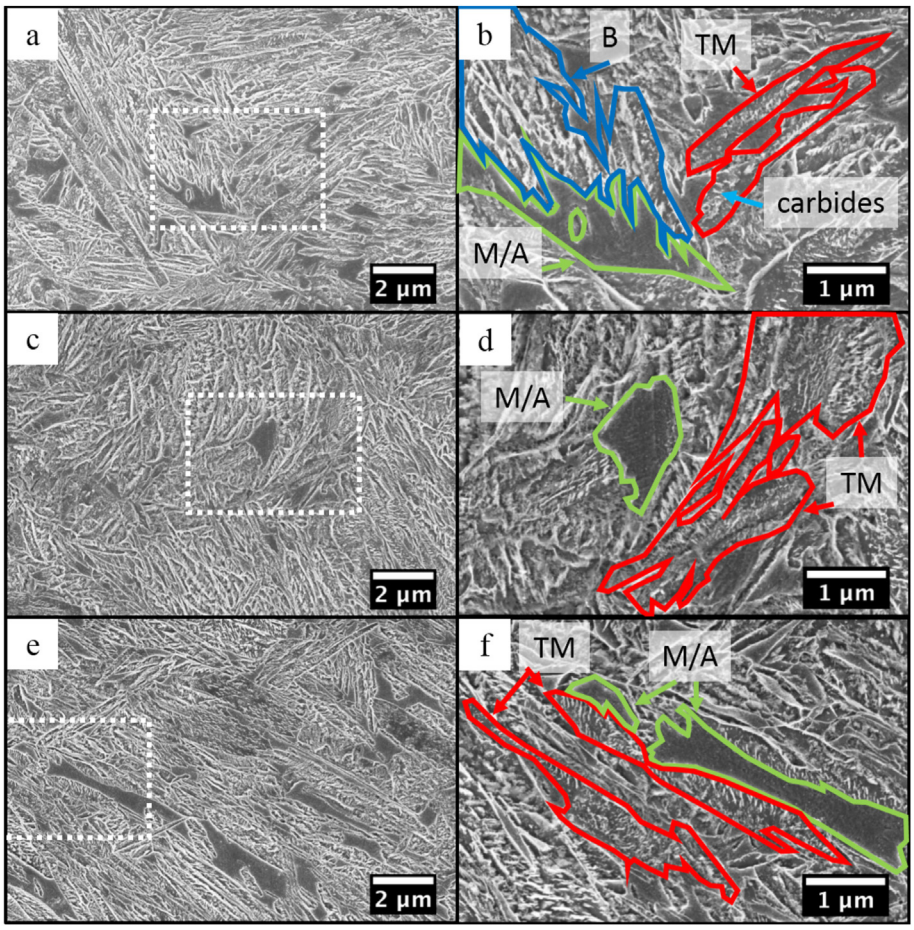

Fig. 6 – SEM micrographs (in-lens) of rolled and DQ&P furnace cooled "coiled" steels: High-Si a)-b), Med-Si c)-d), and Low-Si steels e)-f). Magnified view of dashed rectangles in a), c), and e) are shown in b), d), and f), respectively.

can still be present at the austenite/martensite interfaces. To discern local strain gradients, Kernel average misorientation (KAM) analysis was carried out, as outlined below.

Fig. 8a, d and g present the orientation relationship of Gleeble simulated Q&P specimens for High-, Med- and Low-Si steels, respectively, illustrated via EBSD inverse pole figure (IPF) maps superimposed with image quality (IQ) maps. EBSD phase maps of corresponding specimens are presented in Fig. 8b, e and h, respectively. In the phase maps, red colour corresponds to the finely divided RA blocks/films, whereas the dark grey colour corresponds to martensite. Due to limiting resolution (~80 nm) of the EBSD technique, film-like RA is indexed only partly and usually with lower confidence index. Furthermore, a high dislocation density at the RA/martensite interface leads to low Kikuchi pattern quality. Still, thin strips of film-like residual austenite are discernible, located between martensitic laths and dispersed randomly in all the steels. Qualitatively, a higher fraction of submicron-sized RA was present in High-Si steel with 1.5% Si, in comparison Med-Si (0.68% Si) and Low-Si steel (0.25% Si), thus corroborating the XRD results (Table 2). There was no evidence of the presence of any blocky austenite islands in any of the steels.

In order to quantify the local grain misorientation due to lattice distortion, Kernel average misorientations (KAM) of corresponding specimens were measured and are presented in Fig. 8c, f, and i, respectively, for High-, Med- and Low-Si steels. The KAM maps of the Gleeble simulated Q&P specimens exhibit a significant variation in the local misorientation within highly distorted martensite lath boundary regions. This signifies the local variation of dislocation density in the matrix. Furthermore, KAM in martensite is expectedly higher than in austenite or bainite, highlighted as lenticular phase in blue colour specifying near-zero KAM values.

Fig. 9a, d and g depict the representative IPF maps superimposed with IQ maps of lab rolled DQ&P furnace cooled specimens of High-, Med- and Low-Si steels, respectively, illustrating the orientation distributions revealed by EBSD measurements. Relatively finer PAG packet sizes as well as lath thicknesses, as compared to Gleeble simulated Q&P specimens (Fig. 8a, d and g), and also, a more random orientation distributions can clearly be established from Fig. 9a, d and g (note the higher magnification of images compared to those shown in Fig. 8). This corroborates also a higher total rolling reduction. In the case of Gleeble simulations, total true

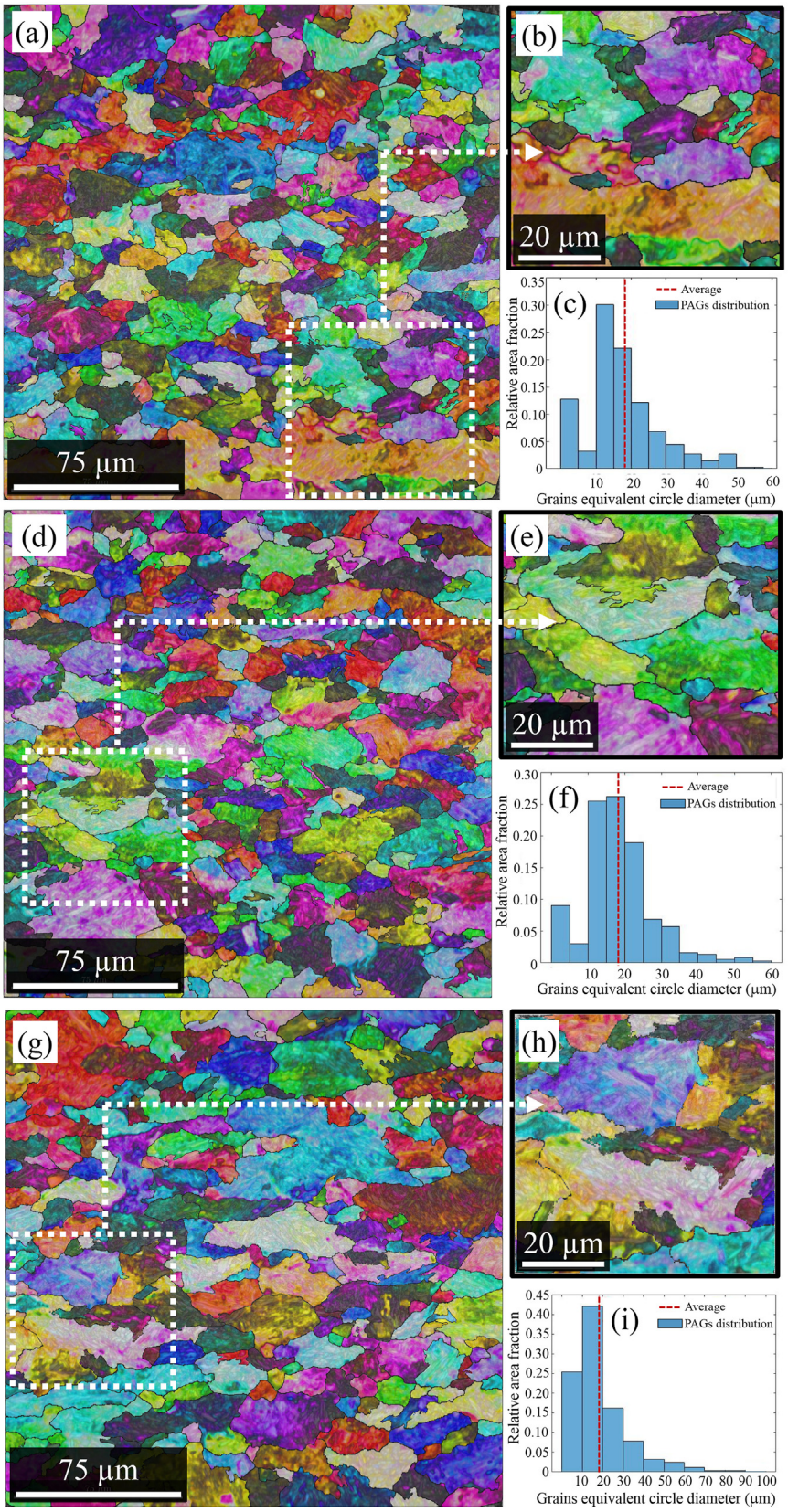

Fig. 7 – Reconstructed PAGs of lab rolled DQ&P steels furnace cooled "coiled", a) High-Si, d) Med-Si and g) Low-Si steels. Magnified view of dashed rectangles in a), d), and g) are shown in b), e), and h), respectively. The corresponding relative area fractions are plotted as bar charts for different PAGs equivalent circle diameters (c, f and i).

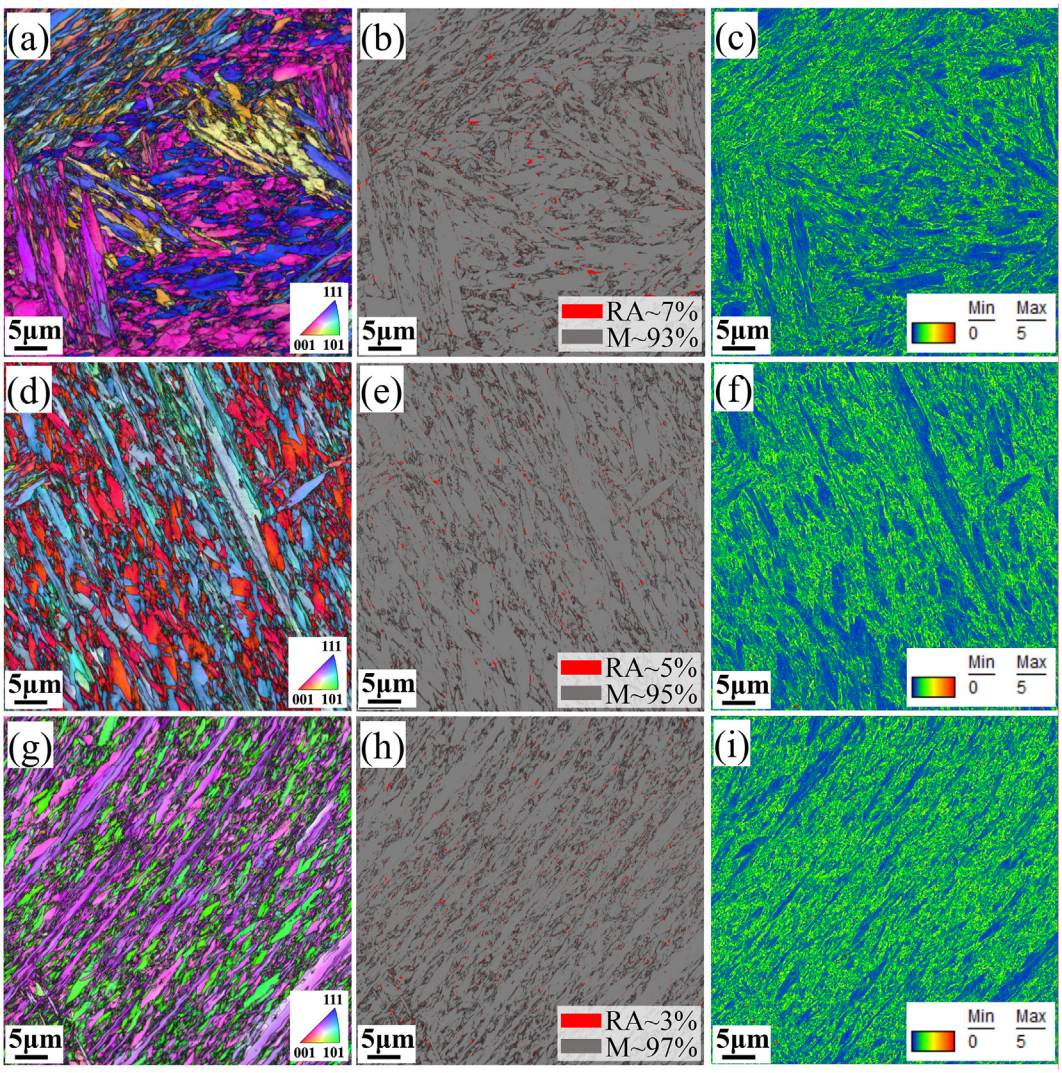

Fig. 8 – EBSD IPF + IQ maps (a,d,g), phase maps (b,e,h) and KAM maps (c,f,i) of Gleeble simulated Q&P samples (T_P/P_t = 200 °C/1000 s) of High-, Med- and Low-Si steels, respectively.

compressive strain (ε) applied at 850 °C was ~0.6, (i.e., 3 × 0.2 straining; equivalent to 45% reduction in thickness), whereas laboratory rolled DQ&P samples experienced a total of ε = ~1.6 (equivalent to 80% rolling reduction), of which about ~0.8 (equivalent to 55% rolling reduction) was in the second stage largely corresponding to no-recrystallization regime, Fig. 2. Phase maps of corresponding DQ&P specimens (High-, Med- and Low-Si steels) are presented in Fig. 9b, e and h, respectively. Although, the trend of RA fractions (15, 13 and 12% for High-, Med- and Low-Si steels, respectively) are within a narrow range and follow a trend in respect of Si contents of the steels (as estimated from XRD measurements, Table 2), the RA fractions obtained via EBSD phase mapping is significantly lower than that measured by XRD, obviously due to the limitation of resolution of the technique. The presence of a relatively higher amount of dislocations in rolled specimens (as also noticed in KAM maps, Fig. 9c, f, and i) leads to somewhat lower quality of Kikuchi patterns. As a result, EBSD measurements could not clearly resolve fine RA films and required a detailed analysis by transmission electron microscopy (TEM).

3.3.3. *TEM analysis*

TEM bright field imaging along with selected area electron diffraction (SAED) patterns characterize the morphology of RA, martensite as well as different carbide precipitates (Fig. 10 a-i). Highly dislocated martensite laths are separated by fine films-like RA clearly revealed in both bright field (Fig. 10a, d, and g) as well as dark field images (Fig. 10b, e, and h). The corresponding SAED patterns of RA were recorded on the [110] zone axis (Fig. 10c, f, i), whereas SAED patterns of martensitic ferrite were recorded on the [111] zone axis. Again, the presence of a relatively higher fraction of RA was evident in High-Si steel, compared to Med- and Low-Si steels, as shown in Fig. 10b, e, and h, respectively. Twinned martensite structure could be identified (Fig. 10a) in some locations in High-Si steel and these must have formed from carbon-enriched austenite during the final cooling, as the martensitic transformation in

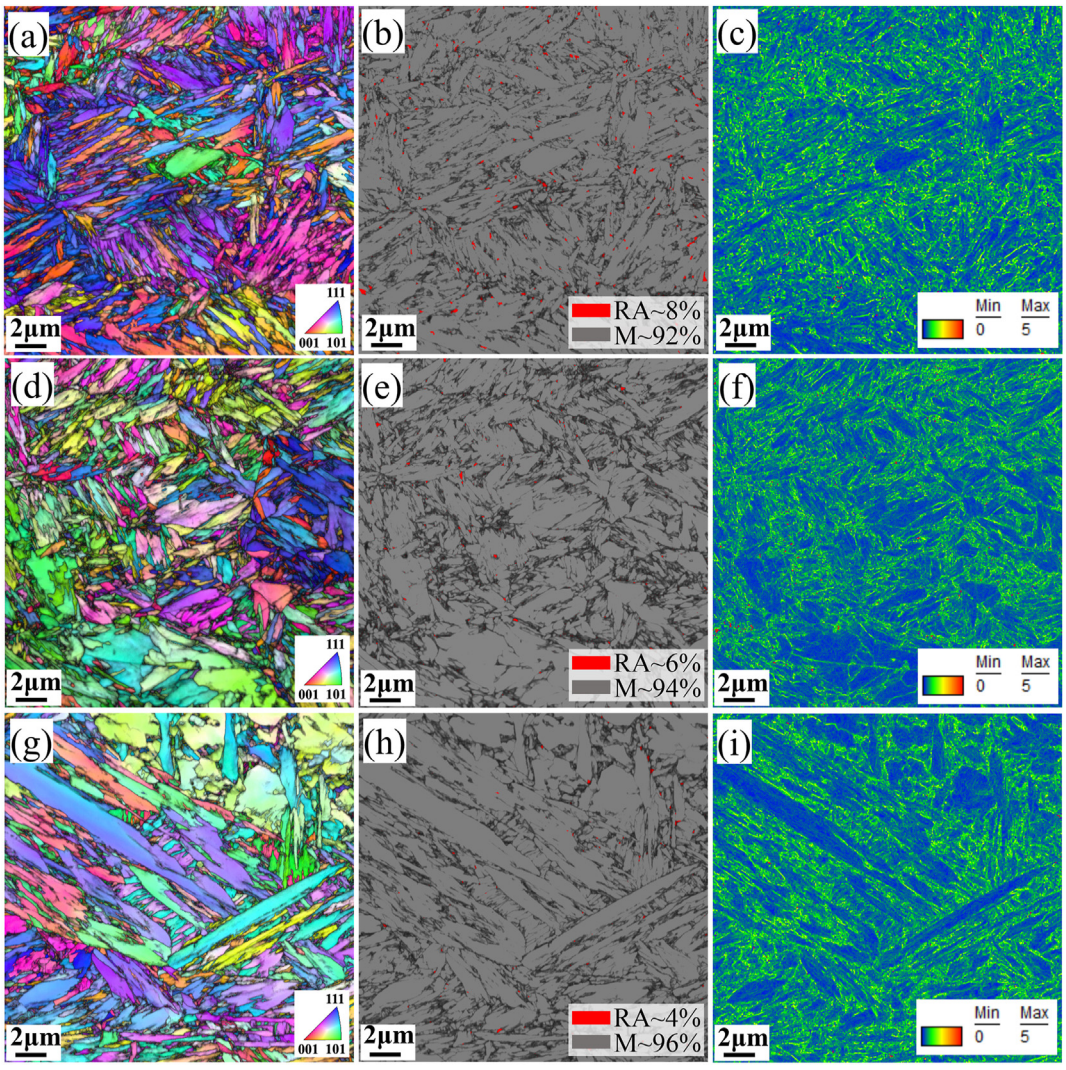

Fig. 9 – EBSD IPF + IQ maps (a,d,g), phase maps (b,e,h) and KAM maps (c,f,i) of laboratory rolled DQ&P furnace cooled samples of High-, Med- and Low-Si steels, respectively.

medium/high carbon steels often accompanies formation of twins to accommodate the transformation strains [31].

Nanosized fine carbides were present within the martensitic laths of both High-, Med- and Low-Si steels, as shown in Fig. 11a, d, and g, respectively. The SAED pattern of the detected carbide precipitates revealed the orthorhombic η-carbide structure (Fig. 10c, f, and i). The interplanar spacing measured from the SAED pattern on [101] [121] and [001] zone axis confirmed the formation of η-carbide. However, any formation of interlath cementite was not observed in any of the samples including Low-Si steel. Qualitatively, the fraction of η-carbide increased gradually from High-Si steel to Low-Si steel.

Overall, these observations suggest that Si acts as a potential graphitizer thus enabling austenite stabilization via promoting carbon partitioning from supersaturated martensite to untransformed austenite. Si-alloying, therefore, is very effective in suppressing the formation of cementite, although seemingly it has a lesser effect on transition carbide precipitation. Earlier studies showed that a high Si content stabilized ε-carbide [11,20]. In contrast, our study clearly depicts the formation of η-carbide. In fact, a high-Si content also resulted in a relatively smaller fraction of η-carbide formation, as seen for High-Si steel (Fig. 11a) in comparison with those of Med- and Low-Si steel (Fig. 11d and g). Pierce et al. [21] have also reported the formation of η-carbide in a 0.38C-1.54Mn-1.48Si steel after quenching at 225 °C, though the partitioning temperature was significantly higher at 400 °C. This also suggests that the presence of a high level of Si in the steel can certainly suppress or delay the carbide formation, but may not completely inhibit it during longer holding at a given partitioning temperature, particularly in the case of medium carbon steels.

3.4. *Mechanical properties*

Tensile properties and impact toughness of laboratory rolled DQ and DQ&P samples from High-, Med- and Low-Si steels (both partitioned at $T_P/P_T = 200$ °C/1000 s and furnace-cooled)

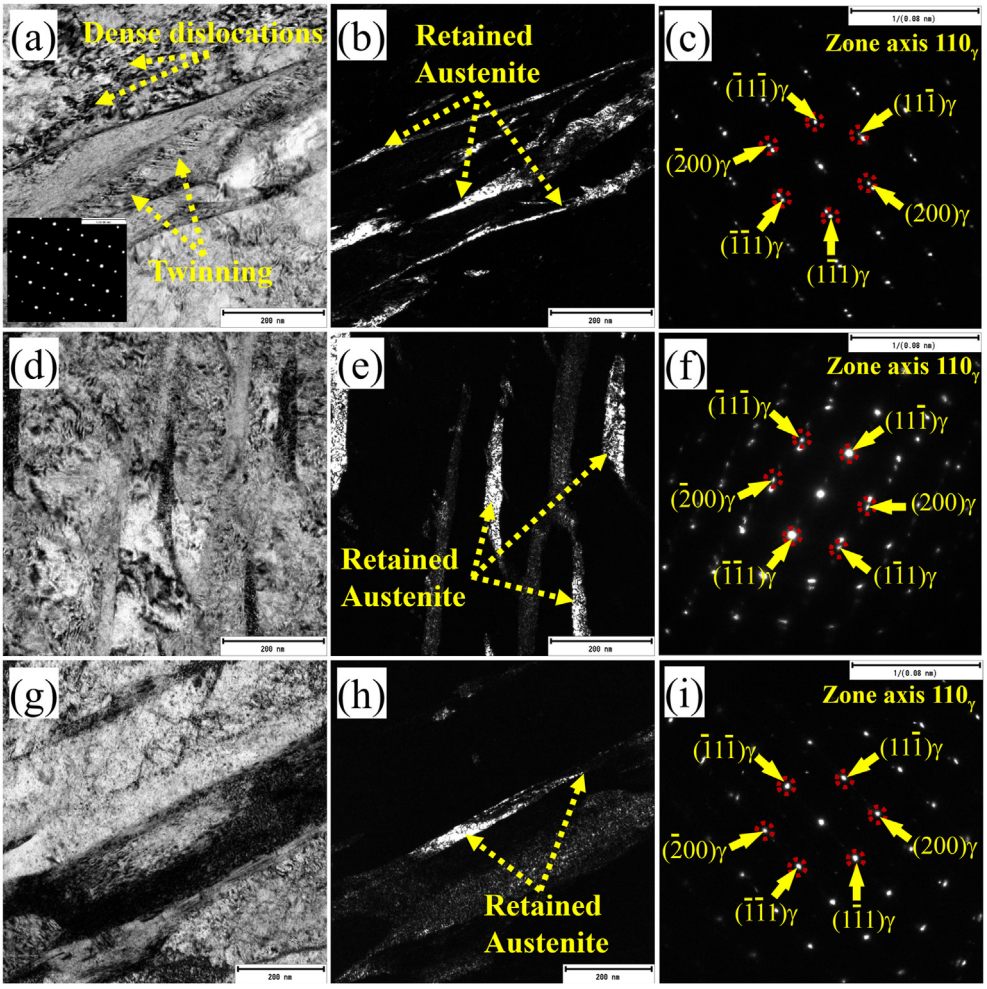

Fig. 10 – TEM bright field (a, d, and g) and dark field (b, e, and h) images and corresponding SAED patterns (c, f, and i) recorded on laboratory rolled DQ&P samples (T_P/P_T = 200 °C/1000 s) of High-, Med- and Low-Si steels, respectively.

are summarized in Table 3. The actual FRTs and T_Q's of the laboratory rolled DQ and DQ&P processed plates are also included in Table 3. Evidently, the laboratory rolling and water quenching lead to some variation in the FRT and T_Q temperatures due to the manual handling of samples. The true stress – true strain curves of all the rolled materials are presented in Fig. 12a, b. The work-hardening rate of the corresponding specimens as a function of true strain are presented in Fig. 12c, d. The merits of DQ&P processing over DQ in respect of both total and uniform elongations are clearly evident from the Fig. 12a, b. Furthermore, DQ&P samples clearly exhibited a particular stage, where the work-hardening rate increased with increasing strain, as compared to DQ specimens. This is attributed to the desired presence of a significant fraction of RA and its stability, thus ensuring the continuous transformation induced plasticity (TRIP) effect. This effect relieves the local stress concentration, delays the initiation of microcracks and thereby enhances the ductility [32–34].

The DQ variant of all three steels have ultrahigh yield strength ($R_{p0.2}$>1400 MPa) together with extremely high tensile strength (R_m > 2500 MPa), though the total elongations of those DQ variants are limited to ~4–5%. In contrast, a short time partitioning of P_T = 1000 s of DQ&P specimens already resulted in reasonable total (A ~10–11%) and uniform (A_g ~6%) elongations, though at a marginally reduced strength level (Table 3), and corroborate the observed microstructure comprising presence of a small fraction of finely divided RA in martensite, Fig. 3. The $R_{p0.2}$ is in accord with the target level (≥1200 MPa) together with tensile strength R_m > 2300 MPa, which is appreciably higher than the target level of 2200 MPa. On the other hand, furnace-cooled DQ&P variants displayed $R_{p0.2}$ (918–1072 MPa), somewhat lower than the target level, although these samples possessed highest total (A ~12–13%) and uniform (A_g ~7%) elongations as a consequence of reduced $R_{p0.2}$ (by ~200–300 MPa) and R_m (by ~250–350 MPa). In particular, tensile strengths were marginally lower for Low-Si steel (Fig. 12 and Table 3) suggesting that at least ~0.7% Si needs to be added to steel plates/strips that are to be partitioned during slow cooling. However, it can also be expected that temper rolling during industrial practice would raise the yield strength to the desired levels (e.g., corresponding to 1.0% proof strength ($R_{p1.0}$) >1300 MPa, (Table 3).

Despite the low T_Q (~150 °C) and T_P (~200 °C) temperatures employed in DQ&P processing, both A_g and A were

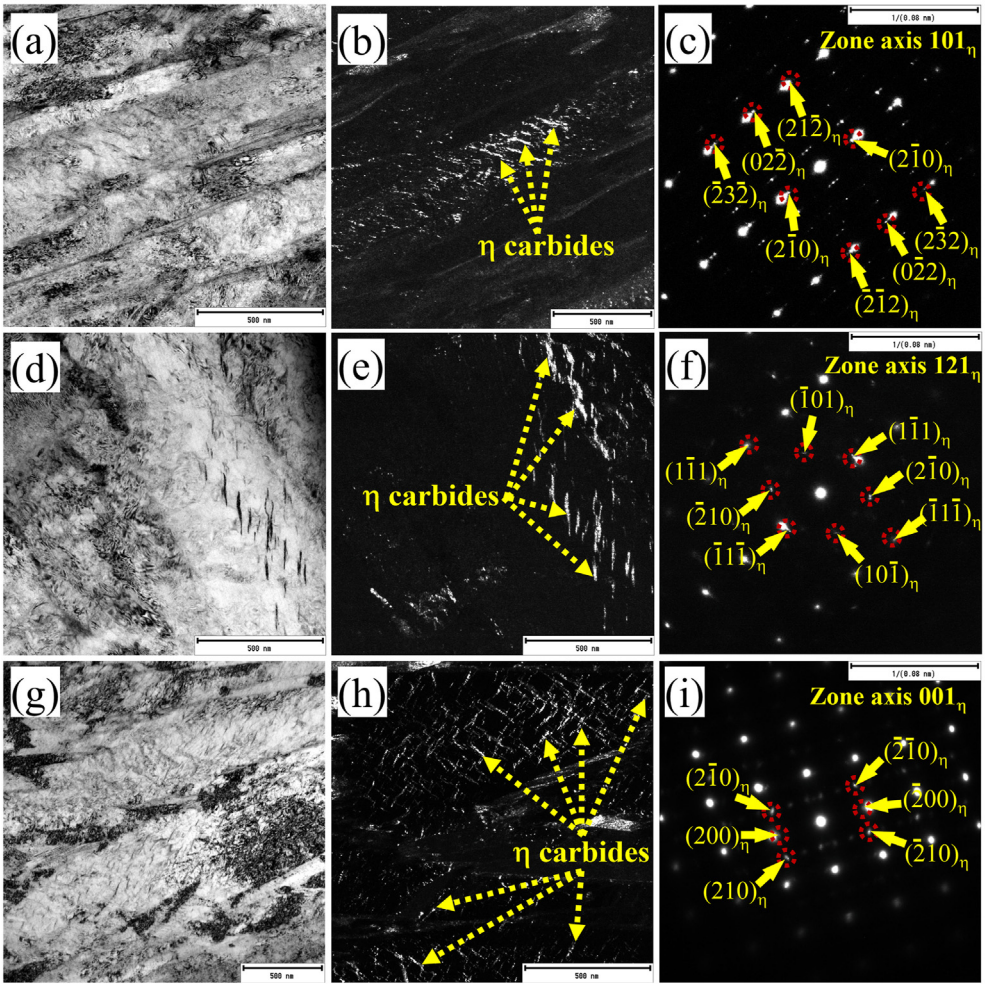

Fig. 11 – TEM bright field (a,d,g) and dark field (b,e,h) images and corresponding SAED patterns (c,f,i) recorded on laboratory rolled DQ&P samples (T_P/P_T = 200 °C/1000 s) of High-, Med- and Low-Si steels, respectively.

satisfactory regardless of the steel composition, suggesting that the given partitioning treatment was effective at such low temperatures in stabilizing appreciable fractions (~12–15%) of RA, Table 2. Also, it resulted in reasonable TRIP strains despite only moderate enrichment (C_γ = ~0.60%), even though all RA may not transform, both due to size effects as well as the possibility of mechanical stabilization. Overall, not only the high strength levels, but also good work hardening capacity and uniform elongations are attributed to the formation of desired nano-lath martensite and finely divided, film-like interlath RA (~12–15%) structures due to DQ&P processing.

Referring to Table 3, a high austenite content resulted in low strength and hardness with a concomitant increase in

Table 3 – Realized final rolling (FRT) and quenching (T_Q) temperatures, and tensile properties of the investigated DQ&P steels. Impact energy at ambient is included in the table.

Code	P_t, s	FRT [°C]	T_Q [°C]	$R_{p0.2}$ [MPa]	$R_{p1.0}$ [MPa]	R_m [MPa]	A [%]	A_g [%]	CV 20 °C [J]
High-Si	DQ	815 ± 5	20	1431 ± 35	–	2537 ± 57	4 ± 0.5	2.5 ± 0.3	9 ± 2
	DQ&P-1000s	805 ± 6	135	1229 ± 41	1682 ± 22	2387 ± 45	10.7 ± 0.3	6.1 ± 0.1	13 ± 1
	DQ&P-FC	825 ± 5	150	926 ± 45	1318 ± 28	2137 ± 49	12.3 ± 0.4	7.3 ± 0.3	28 ± 2
Med-Si	DQ	820 ± 5	20	1457 ± 47	–	2586 ± 36	5.0 ± 0.5	3.7 ± 0.4	6 ± 1
	DQ&P-1000s	820 ± 5	140	1187 ± 14	1684 ± 34	2385 ± 51	10.9 ± 0.5	6.2 ± 0.4	13 ± 2
	DQ&P-FC	815 ± 6	150	918 ± 36	1261 ± 33	2086 ± 44	12.6 ± 0.6	7.1 ± 0.2	31 ± 3
Low-Si	DQ	800 ± 6	20	1477 ± 51	–	2507 ± 53	4.4 ± 0.3	3.1 ± 0.2	7 ± 1
	DQ&P-1000s	810 ± 5	150	1296 ± 29	1691 ± 26	2359 ± 38	10.3 ± 0.8	6.1 ± 0.5	16 ± 2
	DQ&P-FC	820 ± 5	135	1072 ± 57	1360 ± 41	1984 ± 43	13.5 ± 0.7	7.0 ± 0.6	33 ± 3

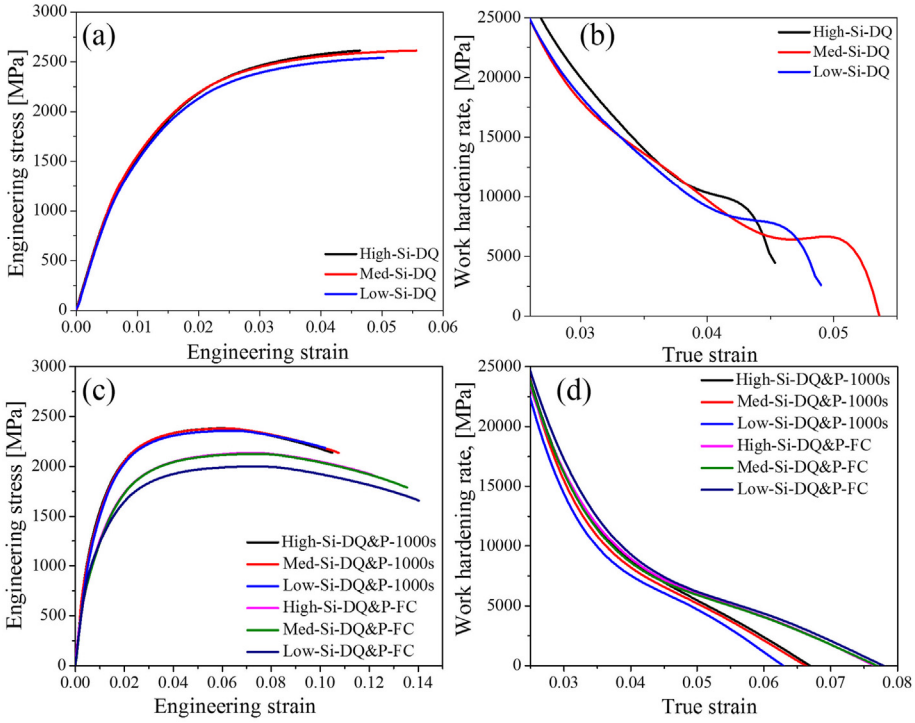

Fig. 12 – True stress - true strain curves of (a) DQ and (b) DQ&P specimens plotted from the engineering stress–strain data from tensile tests, (c,d) work-hardening rate *vs.* true strain for the corresponding samples.

elongation. A part of this difference is also due to nearly absent fresh, high-carbon martensite in the furnace-cooled samples, unlike in the case of samples partitioned just for 1000 s, as also revealed experimentally in Gleeble simulations, Fig. 3c. High-carbon martensite does increase the strength and hardness, Table 3. Interestingly, Low-Si steel showed lowest tensile strength and highest ductility among the furnace-cooled materials, even though it had the lowest RA, presumably because of low tempering resistance due to low Si in the steel [35].

Figure 13 presents the results of the Charpy V impact testing of the laboratory rolled steels. The impact energies of both the DQ versions, and the DQ&P plates quenched and partitioned for 1000 s as well as those slowly cooled in furnace overnight are included in the Fig. 13 as a function of impact testing temperature. Both the DQ samples as well as DQ&P plates corresponding to $T_p/P_T = 200\ °C/1000\ s$ had low impact toughness with energies recorded well below the 28 J impact toughness transition temperature (T_{28J}) criterion even at 100 °C. For the furnace-cooled DQ&P samples, the T_{28J} level was estimated to be between −5 °C and 12 °C, which is rather good for the given strength level achieved in an experimental material processed in a laboratory. With better possibilities of control in industrial practice, the toughness is expected to improve with T_{28J} temperature to be much lower than what observed here. However, there seem to be no clear differences between the three experimental steels regardless of the silicon content, although High-Si showed slightly lower impact energies at higher temperatures with the given sampling, though the data are limited and somewhat scattered. It also possessed the highest strength among the furnace-cooled plates, which can explain the difference.

3.4.1. *Mechanical stability of austenite*

Figure 14 shows the plots of residual austenite content (vol. %) as a function of strain, measured after interrupted tensile tests of FC steels from the middle of cross-sections with tests interrupted at 2%, 6% and 10% engineering strains. It is clear that High-Si steel, which has the highest amount of RA in the beginning, transforms more slowly to provide a given TRIP strain, with the remaining untransformed RA still being highest after 10% strain. High-Si retains about half (~53%) of the original RA (~8 vol. %) amount after just 2% strain, while Med- and Low-Si retain about 29% (~4 vol. %) and 40% (~5 vol. %), respectively. That is, ~9 and 7 vol.% of RA are already consumed during first 2% straining. After 10% strain, High-Si

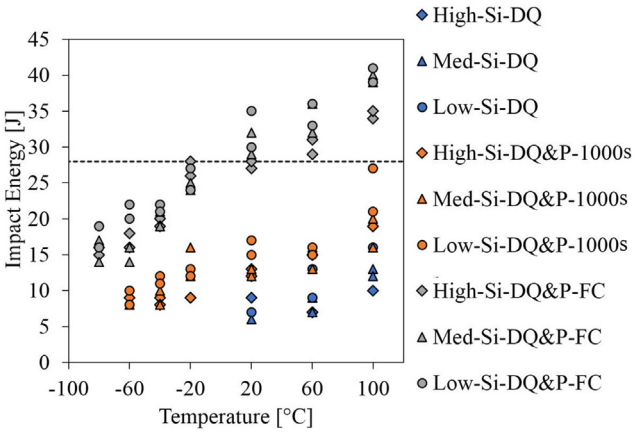

Fig. 13 – Charpy V transition curves of the rolled strips (dashed line at the 28J).

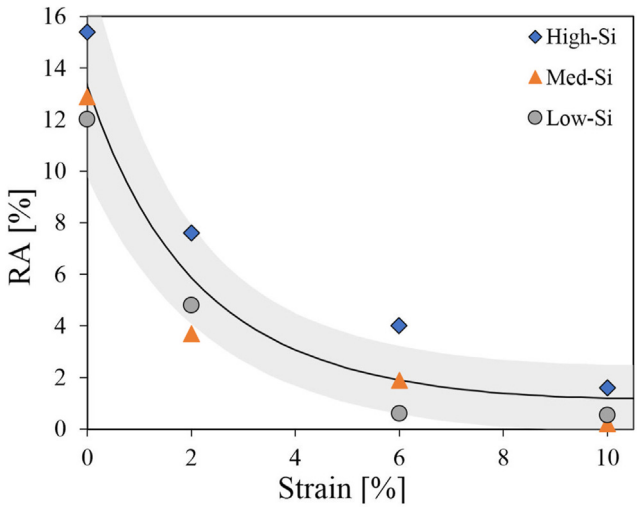

Fig. 14 – Retained austenite fraction after interrupted tensile test of the furnace cooled (FC) samples. The solid line shows the average trend for the three steels, and the gray band the 95% confidence interval for the trend.

has ~2 vol. % of the original RA left, while Med-Si and Low-Si retain only ~0.5 and 1 vol.% RA, respectively. This apparently indicates that the austenite in the High-Si steel has relatively higher mechanical stability. Alternatively, it can also be said that RA has become mechanically more stable when relatively lesser absolute fraction of RA is transformed to attain same amount of deformation strain. It is to be noted that High-Si had higher RA content (~15%) in the unstrained condition. However, already ~13 vol.% (15–2 vol.% RA) of RA was used up to attain just 10% strain in the case of High-Si, while about 12.5 vol.% (13–0.5 vol.% RA) and 11 vol.% (12–1 vol.% RA) of RA fractions were transformed in the case of Med-Si and Low-Si, respectively, to reach the same amount of plastic strain (10%). In effect, Low-Si showed relatively higher stability compared to the other two steels, thus attaining 10% strain with transformation of relatively lower RA fraction (11 vol.%).

The application of straining during interrupted tensile tests normally results in strain partitioning between RA and martensite to different extent [35,36]. Defects such as dislocations in RA can contribute to the nucleation and formation of martensite [35,36]. This effect somewhat compensates the carbon enrichment within RA, which is intended to stabilize against possible strain induced martensite transformation. The starting carbon contents of undeformed specimens, prior to tensile testing were 0.63% and 0.61%, respectively, for High-Si and Low-Si steels, as presented in Table 4. Following 10% tensile straining, the average carbon contents of the untransformed austenite fractions for High-Si (2 ± 0.5 vol. % γ) and Low-Si (1 ± 0.5 vol. % γ) steels, were found to be practically same, i.e., 0.99% C and 1.04% C, respectively, suggesting nearly complete strain induced martensitic transformation in these steels. The untransformed austenite with the highest carbon contents, in general, is considered to be the most stable one. In present study, Low-Si steel exhibited somewhat better mechanical stability despite its low Si content (0.25%). This is attributed to the appreciable decomposition of RA into bainite in the course of partitioning treatment despite low temperature of partitioning (200 °C). As bainite forms, it expels carbon across the transformation boundary, thereby increasing the carbon concentration of the untransformed RA, thereby increasing the stability of the austenite. In Q&P steels, carbon enrichment of the surrounding austenite due to bainite reaction despite low partitioning temperature has also been reported by Nishikawa et al. [37]. Somewhat better mechanical stability of RA in Low-Si steel resulted in relatively higher strain hardening response, as shown in Fig. 12d.

4. Conclusions

This study considers microstructural mechanisms operating in 0.4% carbon steels containing Si in the range 0.25–1.5 wt.%, on subjecting to Q&P simulations in a Gleeble thermomechanical simulator followed by DQ&P simulations in a laboratory rolling mill. Based on the simulation results, a suitable DQ&P processing route comprising multi-pass thermomechanical rolling followed by direct-quenching and partitioning, was designed to achieve the targeted mechanical properties, and is considered to be amenable for industrial processing.

The following conclusions were made:

i) Dilatometric measurements together with detailed microstructural characterization provided an insight about the possible mechanisms, operating in parallel or

Table 4 – Fraction of retained austenite at different amount of strain levels together with their average carbon contents.

Steel code	Processing	Engineering strain [%]	γ [%]	a_γ [Å]	C_γ [%]
High-Si	DQ&P-FC	0	15 ± 1	3.587 ± 0.004	0.63 ± 0.03
		2	8 ± 1	3.598 ± 0.002	0.87 ± 0.02
		6	4 ± 1	3.599 ± 0.003	0.90 ± 0.03
		10	2 ± 0.8	3.603 ± 0.002	0.99 ± 0.05
Med-Si	DQ&P-FC	0	13 ± 1	3.586 ± 0.002	0.59 ± 0.02
		2	4 ± 1	3.589 ± 0.003	0.68 ± 0.03
		6	2 ± 0.5	3.598 ± 0.003	0.88 ± 0.03
		10	0	–	–
Low-Si	DQ&P-FC	0	11 ± 1	3.586 ± 0.005	0.61 ± 0.02
		2	5 ± 1	3.599 ± 0.003	0.90 ± 0.03
		6	1 ± 0.5	3.605 ± 0.002	1.04 ± 0.02
		10	0.8 ± 0.5	–	–

in succession during DQ&P processing, such as carbon partitioning from supersaturated martensite to untransformed austenite, decomposition of austenite into isothermal martensite and/or bainite, and formation of fresh martensite and carbides, etc. with reference to Si content in the steel. The results showed that during holding at 200 °C, tempering of martensite competes with carbon partitioning and bainite transformation.

ii) The carbon content of retained austenite increased with increasing partitioning time at all Si levels. After final cooling, formation of untempered and twinned martensite, was observed in all steels, as identified through TEM study.

iii) DQ&P treatment generates a fine acicular aggregate of carbon-depleted, highly refined martensitic nano-lath structures together with finely divided interlath retained austenite films. Even at a relatively low quench-stop temperature (~150 °C) and partitioning temperature (~200 °C), most of the untransformed austenite could be retained at RT (~12–15%), indicating effective partitioning at given temperature. Despite relatively high carbon (0.4% C) content in the steels, the formation of fine packets of PAGs and fine division of interlath RA films between the martensite laths following slow cooling during DQ&P-furnace-cooling treatment contributed to a very good combination of mechanical properties, including reasonably good ductility and impact toughness.

iv) Formation of transition carbides, though not desirable, could not be prevented with partitioning at temperatures as low as 200 °C, even in the case of steel with highest Si fraction (1.5%). As expected, cementite that forms normally at temperatures much above 250 °C was not observed in any of the samples, regardless of the Si content. However, small fractions of orthorhombic-type η-carbide (Fe_2C) did form during holding for long durations at 200 °C and the precipitate fraction increased with the decrease of Si content in the steel. In general, Si acts as a potent graphitizer, thus enabling austenite stabilization via carbon partitioning from supersaturated martensite, though its effect is less pronounced on transition carbide precipitation at low partitioning temperatures and longer holding times.

Data availability statement

All data are available upon reasonable request by contacting the corresponding author.

Declaration of competing interest

The authors declare that they have no known competing financial interests or personal relationships that could have appeared to influence the work reported in this paper.

Acknowledgement

The authors express their gratitude to the Academy of Finland to provide resources under the auspices of the Genome of Steel (Profi3) project #311934. Technical discussions held with Prof. (Emer.) David A. Porter in designing the alloys are thankfully acknowledged. The authors would also like to thank Mr. Jussi Paavola for assistance in laboratory rolling simulations, Mr. Juha Uusitalo for performing the Gleeble simulation experiments, and Mr. Sami Saukko for the TEM study.

REFERENCES

[1] Speer J, Matlock DK, De Cooman BC, Schroth JG. Carbon partitioning into austenite after martensite transformation. Acta Mater 2003;51:2611–22. https://doi.org/10.1016/S1359-6454(03)00059-4.

[2] Somani MC, Porter DA, Karjalainen LP, Misra DK. Evaluation of DQ&P processing route for the development of ultra-high strength tough ductile steels. Int J Metall Eng 2013;2013:154–60. https://doi.org/10.5923/j.ijmee.20130202.07.

[3] Somani MC, Porter DA, Karjalainen LP, Misra DK. On the decomposition of austenite in a high-silicon steel during quenching and partitioning. Mater Sci Technol 2012;2:1013–20. 2012, MS T 2012.

[4] Xu Y, Tan X, Yang X, Hu Z, Peng F, Wu D, et al. Microstructure evolution and mechanical properties of a hot-rolled directly quenched and partitioned steel containing proeutectoid ferrite. Mater Sci Eng 2014;607:460–75. https://doi.org/10.1016/j.msea.2014.04.030.

[5] Karam-Abian M, Zarei-Hanzaki A, Abedi HR, Heshmati-Manesh S. Micro and macro-mechanical behavior of a transformation-induced plasticity steel developed by thermomechanical processing followed by quenching and partitioning. Mater Sci Eng 2016;651:233–40. https://doi.org/10.1016/j.msea.2015.10.116.

[6] Edmonds DV, de Moor E, Matlock DK, Speer JG. Quenching and partitioning steel, encycl. Iron, steel, their alloy. 2016. p. 2776–93. https://doi.org/10.1081/e-eisa-120048860.

[7] Ghosh S, Miettunen I, Somani MC, Kömi J, Porter D. Nanolath martensite-austenite structures engineered through DQ&P processing for developing tough, ultrahigh strength steels. Mater Today Proc 2021;46:2131–4. https://doi.org/10.1016/j.matpr.2021.02.344.

[8] Edmonds DV, He K, Rizzo FC, De Cooman BC, Matlock DK, Speer JG. Quenching and partitioning martensite-A novel steel heat treatment. Mater Sci Eng 2006;438–440:25–34. https://doi.org/10.1016/j.msea.2006.02.133.

[9] Somani MC, Porter DA, Karjalainen LP, Suikkanen PP, Misra RDK. Process design for tough ductile martensitic steels through direct quenching and partitioning. Mater Today Proc 2015;2:S631–4. https://doi.org/10.1016/j.matpr.2015.07.363.

[10] Kantanen P, Somani M, Kaijalainen A, Haiko O, Porter D, Kömi J. Microstructural characterization and mechanical properties of direct quenched and partitioned high-aluminum and high-silicon steels. Metals 2019;9. https://doi.org/10.3390/met9020256.

[11] Santofimia MJ, Zhao L, Petrov R, Kwakernaak C, Sloof WG, Sietsma J. Microstructural development during the quenching and partitioning process in a newly designed low-carbon steel. Acta Mater 2011;59:6059–68. https://doi.org/10.1016/j.actamat.2011.06.014.

[12] Santofimia MJ, Petrov RH, Zhao L, Sietsma J. Microstructural analysis of martensite constituents in quenching and partitioning steels. Mater Char 2014;92:91–5. https://doi.org/10.1016/j.matchar.2014.03.003.

[13] HajyAkbary F, Sietsma J, Miyamoto G, Furuhara T, Santofimia MJ. Interaction of carbon partitioning, carbide

precipitation and bainite formation during the Q&P process in a low C steel. Acta Mater 2016;104:72–83. https://doi.org/10.1016/j.actamat.2015.11.032.
[14] Da Silva EP, De Knijf D, Xu W, Föjer C, Houbaert Y, Sietsma J, et al. Isothermal transformations in advanced high strength steels below martensite start temperature. Mater Sci Technol 2015;31:808–16. https://doi.org/10.1179/1743284714y.0000000719.
[15] Toji Y, Miyamoto G, Raabe D. Carbon partitioning during quenching and partitioning heat treatment accompanied by carbide precipitation. Acta Mater 2015;86:137–47. https://doi.org/10.1016/j.actamat.2014.11.049.
[16] Somani MC, Porter DA, Karjalainen LP, Misra RDK. On various aspects of decomposition of austenite in a high-silicon steel during quenching and partitioning. Metall Mater Trans A Phys Metall Mater Sci 2014;45:1247–57. https://doi.org/10.1007/s11661-013-2053-8.
[17] Kim DH, Speer JG, Kim HS, De Cooman BC. Observation of an isothermal transformation during quenching and partitioning processing. Metall Mater Trans A Phys Metall Mater Sci 2009;40:2048–60. https://doi.org/10.1007/s11661-009-9891-4.
[18] van Bohemen SMC, Santofimia MJ, Sietsma J. Experimental evidence for bainite formation below Ms in Fe-0.66C. Scripta Mater 2008;58:488–91. https://doi.org/10.1016/j.scriptamat.2007.10.045.
[19] Santofimia MJ, Zhao L, Sietsma J. Volume change associated to carbon partitioning from martensite to austenite. Mater Sci Forum 2012;706–709:2290–5. https://doi.org/10.4028/www.scientific.net/MSF.706-709.2290.
[20] Miettunen I, Ghosh S, Somani MC, Pallaspuro S, Kömi J. Competitive mechanisms occurring during quenching and partitioning of three silicon variants of 0.4 wt.% carbon steels. J Mater Res Technol 2021. https://doi.org/10.1016/j.jmrt.2021.01.085.
[21] Waterschoot T, Verbeken K, De Cooman BC. Tempering kinetics of the martensitic phase in DP steel. ISIJ Int 2006;46:138–46. https://doi.org/10.2355/isijinternational.46.138.
[22] Speer JG, Assunção FCR, Matlock DK, Edmonds DV. The "quenching and partitioning" process: background and recent progress. Mater Res 2006;8:417–23. https://doi.org/10.1590/s1516-14392005000400010.
[23] Santofimia MJ, Zhao L, Sietsma J. Overview of mechanisms involved during the quenching and partitioning process in steels. Metall Mater Trans A Phys Metall Mater Sci 2011;42:3620–6. https://doi.org/10.1007/s11661-011-0706-z.
[24] De Moor E, Lacroix S, Samek L. Dilatometric study of the quench and partitioning process. In: 3rd Int. Conf. Adv. Struct. Steels.; 2006.
[25] Kim B, Sietsma J, Santofimia MJ. The role of silicon in carbon partitioning processes in martensite/austenite microstructures. Mater Des 2017;127:336–45. https://doi.org/10.1016/j.matdes.2017.04.080.
[26] Kim K, Lee SJ. Effect of Ni addition on the mechanical behavior of quenching and partitioning (Q&P) steel. Mater Sci Eng 2017;698:183–90. https://doi.org/10.1016/j.msea.2017.05.030.
[27] Nyyssönen T, Isakov M, Peura P, Kuokkala V-T. Iterative determination of the orientation relationship between austenite and martensite from a large amount of grain pair misorientations. Metall Mater Trans 2016;47:2587–90. https://doi.org/10.1007/s11661-016-3462-2.
[28] Bachmann F, Hielscher R, Schaeben H. Grain detection from 2d and 3d EBSD data-Specification of the MTEX algorithm. Ultramicroscopy 2011;111:1720–33. https://doi.org/10.1016/j.ultramic.2011.08.002.
[29] Dyson DJ, Holmes B. Effect of alloying additions on the lattice parameter of austenite. J Iron Steel Inst 1970:469–74.
[30] Scott CP, Drillet J. A study of the carbon distribution in retained austenite. Scripta Mater 2007;56:489–92. https://doi.org/10.1016/j.scriptamat.2006.11.033.
[31] Zhang P, Chen Y, Xiao W, Ping D, Zhao X. Twin structure of the lath martensite in low carbon steel. Prog Nat Sci Mater Int 2016;26:169–72. https://doi.org/10.1016/j.pnsc.2016.03.004.
[32] Lee Chang Gil, Kim Sung-Joon, Lee Tae-Ho, Lee Sunghak. Effects of volume fraction and stability of retained austenite on formability in a 0.1C–1.5Si–1.5Mn–0.5Cu TRIP-aided cold-rolled steel sheet. Mater Sci Eng 2004;371:16–23. https://doi.org/10.1016/S0921-5093(03)00035-2.
[33] Zhang Ke, Zhang Meihan, Guo Zhenghong, Chen Nailu, Rong Yonghua. A new effect of retained austenite on ductility enhancement in high-strength quenching–partitioning–tempering martensitic steel. Mater Sci Eng 2011;528:8486–91. https://doi.org/10.1016/j.msea.2011.07.049.
[34] Nam WJ, Choi HC. Effect of Si on mechanical properties of low alloy steels. Mater Sci Technol 1999;15(5):527–30. https://doi.org/10.1179/026708399101506238.
[35] Hidalgo J, Findley KO, Santofimia MJ. Thermal and mechanical stability of retained austenite surrounded by martensite with different degrees of tempering. Mater Sci Eng 2017;690:337–47. https://doi.org/10.1016/j.msea.2017.03.017.
[36] Garcia-Mateo C, Caballero FG, Chao J, Capdevila C, Garcia de Andres C. Mechanical stability of retained austenite during plastic deformation of super high strength carbide free bainitic steels. J Mater Sci 2009;44:4617–24. https://doi.org/10.1007/s10853-009-3704-4.
[37] Nishikawa S, Santofimia Maria J, Sietsma Jilt, Goldenstein Hélio. Influence of bainite reaction on the kinetics of carbon redistribution during the Quenching and Partitioning process. Acta Mater 2018;142:142–51. https://doi.org/10.1016/j.actamat.2017.09.048.